# Simple interpretation of nuclear orientation for Coulomb barrier distributions derived from a realistic effective interaction

M. Ismail and W. M. Seif
*Cairo University, Faculty of Science, Department of Physics, Giza 12613, Egypt*
(Received 8 December 2009; published 23 March 2010)

A simple straightforward method has been presented to predict the dependence of barrier distributions at arbitrary orientations on different deformations. The proposed interpretation is developed independently of the complicated numerical calculations. It is related to the change of half-density radius of the deformed nucleus, in the direction of the separation vector. The microscopic calculations of Coulomb barrier are carried out by using a realistic density dependent nucleon-nucleon ($NN$) interaction, BDM3Y, for the interaction between spherical, $^{48}$Ca, and deformed, $^{244}$Pu, nuclei, as an example. To do so, the double-folding model for the interaction of spherical-deformed nuclei is put in a suitable computational form for the calculation of the potential at several separation distances and orientation angles using the density dependent $NN$ force without consuming computational time. We found that the orientation distributions of the Coulomb barrier parameters show similar patterns to those of the interacting deformed nucleus radius. It is found that the orientation distribution of the Coulomb barrier radius follows the same variation of the deformed nucleus radius while the barrier height distribution follows it inversely. This correlation (anticorrelation) allows a simple evaluation of the orientation barrier distribution which would be very helpful to estimate when the barrier parameters will increase or decrease and at which orientations they will be independent of the deformation. This also allows us to estimate the compact and elongated configurations of the interacting nuclei which lead to hot and cold fusion, respectively.

DOI: 10.1103/PhysRevC.81.034607 PACS number(s): 25.60.Pj, 25.10.+s

## I. INTRODUCTION

Recently, the understanding of the enhancement effects due to nuclear deformations in the different nuclear reactions received particular attention especially in fusion reactions and synthesis of superheavy nuclei (SHN) [1–7]. This supports analyzing and suggests new experiments. It has long been recognized that nuclear deformations affect the Coulomb barrier between the interacting nuclei. The cross section of various nuclear reactions and production of the superheavy elements are controlled by the Coulomb barrier through the barrier penetrability [8–10] and the potential energy surfaces. The different macroscopic and microscopic models [11–18] proposed to understand the production mechanism of SHN through cold [19] or hot [20,21] fusion reactions, confirm the role of deformation. Indeed, the reasonable prediction of the formation cross section of SHN would require knowledge of the interaction potential energy surfaces at different orientations for spherical-deformed and deformed-deformed interacting pairs of nuclei, which essentially influences the competition between fusion and quasifission cross sections.

When one or both of the interacting nuclei are well deformed in their ground states, the microscopic calculation of Coulomb and nuclear contributions of the interaction potential are time consuming where six-dimensional integrals are involved. So, it is desirable to find an alternative simple method to derive the heavy-ion (HI) potential for interacting deformed oriented nuclei with acceptable accuracy. This will help to reduce time consumed in such approaches which need to calculate the interaction potential at different orientations several times such as the coupled-channel method. Different phenomenological methods have been proposed to this aim such as Wong's expression [22] for the Coulomb interaction between two deformed nuclei, considering nonoverlapping densities, and the nuclear proximity potential [23,24] which is frequently used in the most recent SHN studies [24–28]. For microscopic calculations, the double-folding model with a density-dependent finite-range direct part of the nucleon-nucleon ($NN$) interaction, but with simple zero-range exchange part, has been used to generate the HI interaction potential at different orientations [29] giving Coulomb barrier distributions with smooth orientation behavior.

To get the optimum orientations for hot and cold fusion of the colliding nuclei [24], to produce SHN, the role of deformations is of great interest when one or both of the nuclei participating in the reaction are deformed. It is clear that the general behavior of Coulomb barrier parameters, its height and radius, is the key to understanding the role of deformations. The distribution of Coulomb barriers in the orientation degrees of freedom is related in a clear way to the reacting nuclei deformations [25,26], their signs and magnitudes. For instance, while the sign of the quadrupole deformation determines the optimized orientations, it is found that the reacting nuclei may affect the hexadecapole deformation contribution according to the charge number, $Z$, of the produced nucleus [24]. When the interacting deformed nuclei, or one of them, are prolate, it is shown that the lowest barrier is at orientation 0° (180°) [30] which is pole-to-pole configuration (polar configuration in case of spherical-deformed interacting nuclear pair). The belly-to-belly or the equator-cross, equatorial, configuration which is the orthogonal symmetry axes orientation, 90°, gives the most compact configuration [31] that describes the hot fusion reactions. The presence of hexadecapole deformation with small and/or negative values keeps the equatorial-cross

 

compact configuration [25] but it is not the case for the large positive values. An optimized equatorial-cross compact configuration, hot fusion reaction, is attributed to the interacting prolate nuclei with negative or positive hexadecapole deformation for the reactions leading to $Z \geqslant 114$ nuclei. The reaction leading $Z < 114$ is a cold fusion reaction for the deformed nuclei with large positive hexadecapole deformation [25]. Large positive hexadecapole deformation results in nonequatorial compact configurations, with a difference of about 20°, for the $^{48}$Ca + $^{244}$Pu collision. For an oblate nucleus with positive or negative hexadecapole deformation interacting with a spherical one, a compact configuration is obtained at orientation 0° [24] while the elongated configuration is given at the orthogonal orientation, 90°. These results are obtained theoretically using phenomenological approaches, such as the nuclear proximity approach and Wong's expression, and most of them are further experimentally confirmed [11,19,20,32]. The different simple approximate methods used to calculate the HI potential lead to Coulomb barriers that differ considerably for the same colliding system. The uncertainty of the HI potential near the touching point of the two interacting nuclei arises from the different approximations giving rise to a variety of different proposed nuclear reaction mechanisms leading to SHN formation. So, one can decrease this uncertainty by deriving the HI potential microscopically without making severe approximations. In this work we perform a microscopic study using the double-folding model that is based on a zero-range and finite-range density dependent exchange $NN$ interaction part, in addition to the finite-range direct part, to study the deformation and orientation effects on the Coulomb barrier. We try to interpret the behavior of the Coulomb barrier parameters in deformation and orientation degrees of freedom in a simple way. We found that the variation of these parameters follow to a good extent the change of the deformed nucleus radius, $R_T(\beta)$, in the direction of the separation vector joining the centers of mass of the interacting nuclei, $\overrightarrow{R}$. The deformed nucleus radius is given by a simple linear combination of Legendre polynomials, functions of orientation angel ($\beta$), and the deformation parameters of the target nucleus. Consequently, the simple behavior of $R_T(\beta)$ in the orientation degrees of freedom and its deformation parameters dependence could be used to simulate the orientation and deformation parameters variation of the more complicated quantities, barrier height and radius. The relation between the variation of $R_T(\beta)$ and barrier parameters helps to study the following problems:

(i) The compactness of hot fusion reactions between spherical projectiles and deformed target nuclei in the synthesis of superheavy elements (SHE). Compact configuration means highest barrier and smallest barrier radius. The variation of $R_T(\beta)$ in the direction of $\overrightarrow{R}$ for a given spherical-deformed pair of nuclei, according to the orientation of the deformed nucleus and its deformations, could clarify certain aspects of the reaction compactness. It could predict that either the reaction is equatorial compact hot fusion, with the collision in the direction of the minor axis of the deformed nucleus, or it is nonequatorial one, when the compactness occurs at orientation angle less than 90°. This problem depends essentially on the values of deformation parameters.

(ii) The importance of high-order deformation parameters such as $\beta_6$ and $\beta_8$ in calculating the Coulomb barrier parameters. Do they reinforce the contribution of the low-order ones ($\beta_3$ and $\beta_4$) to the quadrupole deformation or do they cancel each other leaving the effect of quadrupole deformation only [27]? Eventually our goal will be to discuss the microscopic results for the orientation dependence of the Coulomb barrier distribution of a spherical-deformed interacting nuclear pair in a simple way through the variation of the deformed nucleus radius. We further investigate to what extent other simple calculations [24–28] describe successfully the Coulomb barrier behavior in the orientation degrees of freedom. We consider the fusion of $^{48}$Ca to $^{244}$Pu, which leads to the formation of the superheavy element $^{292}$114, as an example for the spherical-deformed reacting pair. The recent measured excitation functions for the 4$n$ channel of this reaction was an evidence for the compactness of hot fusion reactions [32].

In the next section, we first describe the details of the extended double-folding formalism we use in the present work to calculate both the nuclear and Coulomb parts of the HI potential for a spherical-deformed interacting nuclear pair. We then present and discuss the obtained results of the orientation barrier distribution for the system $^{48}$Ca + $^{244}$Pu in Sec. III. From this discussion we will show that the variation of the deformed nucleus radius simulates the Coulomb barrier distribution in the orientation degrees of freedom. Finally, the summary and conclusion are presented in the last section.

## II. THEORETICAL FRAMEWORK

In this section we outline the double-folding procedure that will be used to perform the microscopic calculations of the Coulomb and nuclear, direct and exchange, potential parts. We adopt an improved density dependent version, BDM3Y1 [33], of the realistic effective M3Y $NN$ force based on the $G$-matrix elements of the Paris [34] $NN$ potential. The density dependence has been introduced to reproduce the cold nuclear matter saturation properties.

The interaction potential between spherical projectile and deformed target at separation distance, $R$, between their centers is given by

$$U(R,\ \beta) = U_D(R,\ \beta) + U_{\rm Ex}(R,\ \beta). \qquad (1)$$

$\beta$ is the orientation angle of symmetry axis of deformed target nucleus measured from the separation distance vector $\overrightarrow{R}$ between the centers of the interacting nuclei, Fig. 1. The direct, $U_D$, and exchange, $U_{\rm Ex}$, HI potential parts are then given, respectively, as

$$U_D(R,\ \beta) = \int d\vec{r}_1\, d\vec{r}_2 \quad V_D(s,\rho)\ \rho_P(\vec{r}_1)\ \rho_T(\vec{r}_2), \qquad (2)$$

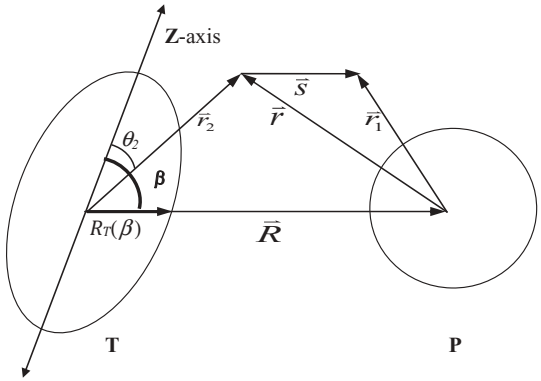


FIG. 1. Schematic representation of the two interacting nuclei shows the coordinate system.

$$U_{Ex}(R,\beta) = \int d\vec{r}_1\, d\vec{r}_2 \quad V_{Ex}(s,\rho)\, \rho_P(\vec{r}_1, \vec{r}_1 - \vec{s}) \times \rho_T(\vec{r}_2, \vec{r}_2 + \vec{s}) e^{\frac{i}{M}\vec{k}(R)\cdot\vec{s}}, \tag{3}$$

where $\vec{s} = \vec{R} + \vec{r}_1 - \vec{r}_2$, Fig. 1. $\rho_P(\vec{r}_1)$ and $\rho_T(\vec{r}_2)$ denote the density distributions for projectile and target, respectively, $V_{D(Ex)}(s,\rho)$ is the direct (exchange) $NN$ force. The local wave number, $|\vec{k}\ (R)|$, is given as

$$|\vec{k}\ (R)|^2 = \frac{2\mu}{\hbar^2}[E_{CM} - U(R,\beta) - U_C(R,\beta)]. \tag{4}$$

$\mu$ is the reduced mass for the reacting nuclei and $U_C$ is their interacting Coulomb potential that also can be calculated by Eq. (2) by replacing the matter density distributions with the charge density distributions and using $\frac{e^2}{s}$ instead of $V_D(s,\rho)$. For each value of the separation distance, R, and the orientation angle, $\beta$, we have to calculate the six-dimensional folding integrals, Eqs. (2) and (3), for both the direct and exchange parts of the nuclear HI potential and for the Coulomb interaction as well. The evaluation of these integrals is an intricate numerical problem. So, we try here to simplify them in a similar way as that used in case of two interacting spherical nuclei. To do so we start by taking the Fourier transforms of the $NN$ force as

$$V_D(s,\rho) = \int e^{i\vec{k}\cdot\vec{R}} e^{i\vec{k}\cdot\vec{r}_1} e^{-i\vec{k}\cdot\vec{r}_2} \tilde{V}_D(k,\rho) d\vec{k}, \tag{5}$$

where

$$\tilde{V}_D(k,\rho) = \frac{1}{(2\pi)^3}\int e^{-i\vec{k}\cdot\vec{r}} V_D(r,\rho) d\vec{r}. \tag{6}$$

The density dependent M3Y-Paris effective $NN$ force considered in the present work, BDM3Yn, has the factorized shape [33,34]

$$V_D(s,\rho) = \left[11061.625\frac{e^{-4s}}{4s} - 2537.5\frac{e^{-2.5s}}{2.5s}\right] F(\rho)g(E), \tag{7}$$

$$V_{Ex}(s,\rho) = \left[-1524.25\frac{e^{-4s}}{4s} - 518.75\frac{e^{-2.5s}}{2.5s} - 7.8474\frac{e^{-0.7072s}}{0.7072s}\right] F(\rho)g(E), \tag{8}$$

with the density and energy dependence, respectively,

$$F(\rho) = c(1 - \gamma\rho^n), \quad g(E) = (1 - 0.003E_{Ap}). \tag{9}$$

The parameters $c$, $\gamma$, and $n$ are adjusted to reproduce normal nuclear matter saturation properties for a given equation of state for cold nuclear matter. For BDM3Y1, $c = 1.2521$, $\gamma = 1.7452$ fm$^3$ and, $n = 1$ which generate nuclear matter equation of state with incompressibility value, $K = 270$ MeV. $E_{Ap}$ is the incident energy per projectile nucleon in the laboratory system.

However, in view of the short range of the effective interaction, it is sufficiently accurate to use the convenient form, $\rho = \rho_T(\vec{r}_1) + \rho_P(\vec{r}_2)$, for the total density, Eq. (9), that underestimate the folded potential up to about 15% in the inner radial region when the projectile penetrates deeply into the target nucleus [35,36]. So, we can express the direct part of the HI potential for the case of density dependent $NN$ force of the form BDM3Yn, $n = 1$, as

$$\begin{aligned} U_D(\vec{R},\beta) &= cg(E)\int d\vec{k}\ \tilde{V}_D(k) e^{i\vec{k}\cdot\vec{R}}\left[\int d\vec{r}_2\, e^{-i\vec{k}\cdot\vec{r}_2}\rho_T(\vec{r}_2)\right. \\ &\times \int d\vec{r}_1\, e^{i\vec{k}\cdot\vec{r}_1}\rho_P(\vec{r}_1) - \gamma\left(\int d\vec{r}_2\, e^{-i\vec{k}\cdot\vec{r}_2}\rho_T^2(\vec{r}_2)\right. \\ &\times \int d\vec{r}_1\, e^{i\vec{k}\cdot\vec{r}_1}\rho_P(\vec{r}_1) + \int d\vec{r}_2\, e^{-i\vec{k}\cdot\vec{r}_2}\rho_T(\vec{r}_2) \\ &\left.\left.\times \int d\vec{r}_1\, e^{i\vec{k}\cdot\vec{r}_1}\rho_P^2(\vec{r}_1)\right)\right]. \end{aligned} \tag{10}$$

$\tilde{V}_D(k)$ is the Fourier transformation of the ordinary M3Y force, the quantity between square brackets in Eq. (7). For spherical projectile nucleus, one can integrate over the angular part of $\vec{r}_1$ to get the one-dimensional integrals,

$$A_P^1(\vec{k}) = 4\pi\int_0^\infty dr_1 r_1^2 j_0(kr_1)\rho_P(r_1), \quad A_P^2(\vec{k}) = 4\pi\int_0^\infty dr_1 r_1^2 j_0(kr_1)\rho_P^2(r_1). \tag{11}$$

On the other hand, by choosing the orientation angle of the symmetry axis in the $z$-axis direction, the integration over $\vec{r}_2$ will be independent of the azimuthal angle, $\phi_2$. So, the three-dimensional integrals over $\vec{r}_2$ become two-dimensional ones. Now, expanding $e^{-i\vec{k}\cdot\vec{r}_2}$ into its multipole components, assuming deformed target with axial symmetry, then defining

$$\begin{aligned} A_T^1(\vec{k}) &= 2\pi\int_0^\infty dr_2 r_2^2 j_\ell(kr_2)\int_0^\pi d\theta_2 \sin\theta_2\rho_T \\ &\times (r_2,\cos\theta_2)Y_{\ell,0}(\cos\theta_2), \\ A_T^2(\vec{k}) &= 2\pi\int_0^\infty dr_2 r_2^2 j_\ell(kr_2)\int_0^\pi d\theta_2 \sin\theta_2\rho_T^2 \\ &\times (r_2,\cos\theta_2)Y_{\ell,0}(\cos\theta_2), \end{aligned} \tag{12}$$

and integrating over the angular part of $\vec{k}$, Eq. (10) becomes

$$U_D(\vec{R},\beta) = 4\pi \sum_{\ell} \mathrm{Y}_{\ell,0}(\vec{R}\cdot\hat{\Omega}) cg(E) \int_0^\infty dk k^2 j_\ell(kR)\tilde{V}_D(k) \times \left[A_T^1(k)A_P^1(k) - \gamma\left(A_T^2(k)A_P^1(k) + A_T^1(k)A_P^2(k)\right)\right]. \quad (13)$$

$\hat{\Omega}$ is in the direction of the symmetry axis of the target nucleus. This expression has several important advantages. The most obvious one is that the six-dimensional integral of the folding potential is reduced to a one-dimensional one over $k$ containing four form factors. Two of them are one-dimensional integrals, $A_P^{1,2}(k)$, while the other two are two-dimensional ones, $A_T^{1,2}(k)$. These form factors are independent of both the separation distance between the reacting nuclei and the orientation angle, $\beta$, so they need to be calculated only once for each $\ell$ value. This allows the calculation of $U_D(\vec{R},\beta)$ at different values of $R$ and $\beta$ without consuming much computational time. Moreover, the orientation dependence is contained only in $\mathrm{Y}_{\ell m}(\vec{R}\cdot\Omega)$ which is outside the integral. On the other hand, the sum over $\ell$ converges rapidly. In the presence of quadrupole and hexadecapole deformations only, $\ell$ takes even values and then one needs five $\ell$ values to get almost exact results. Eventually, this expression, Eq. (13), is simple as that of the HI potential for interacting spherical nuclei [37] except that it involves two-dimensional integrals. In fact, the integration over the nondiagonal densities for projectile and target to calculate the exchange part of the HI nuclear potential, Eq. (3), contains a self-consistency problem where $\vec{k}$ $(R)$ depends on the potential itself, Eq. (4). So, in order to calculate the exchange contribution of the HI potential, we first approximate the nonlocal (one-body) densities using density matrix expansion [38] where the available densities are in the local form. To do so, the nonlocal densities of projectile and target are approximated [39], referring to Fig. 1, as

$$\rho_P(\vec{r}_1,\vec{r}_1-\vec{s}) \cong \hat{j}_1\left(k_{\mathrm{eff}}^p(|\vec{y}-\vec{R}|)s\right)\rho_P(|\vec{y}-\vec{R}|),$$
$$\rho_T(\vec{r}_2,\vec{r}_2+\vec{s}) \cong \hat{j}_1\left(k_{\mathrm{eff}}^T(y,\cos\theta_2)s\right)\rho_T(y,\cos\theta_2,)$$
$$\vec{y} = \vec{r}_2 + \frac{\vec{s}}{2}, \quad \hat{j}_1(x) = \frac{3j_1(x)}{x}, \quad (14)$$

where $j_1$(x) is the first order spherical Bessel function. For a spherically symmetric ground state density, the average local Fermi momentum, $k_{\mathrm{eff}}^i (i = P, T)$, is given in terms of the kinetic energy density, $\tau_i$, as [38]

$$\left|k_{\mathrm{eff}}^i(r)\right|^2 = \left(\frac{3}{5\rho_i}\tau_i(r) - \frac{1}{4}\nabla^2\rho_i(r)\right). \quad (15)$$

Using the extended Thomas-Fermi approximation [39,40], the kinetic energy density is then given by

$$\tau_i(r) = \frac{3}{5}\left(\frac{3\pi^2}{2}\right)^{2/3}\rho_i^{5/3}(r) + \frac{1}{3}\nabla^2\rho_i(r) + \frac{1}{36}\frac{|\nabla\rho_i(r)|^2}{\rho_i(r)}. \quad (16)$$

The first term in this expression stands for Thomas-Fermi approximation while the other two terms represent the surface correction. Inserting the above local approximation, Eq. (14), with the $NN$ density dependent exchange interaction, Eq. (8), into the folding integral, Eq. (3), transforming the integration variables from $\vec{r}_1$ and $\vec{r}_2$ into $\vec{y}$ and $\vec{s}$ (see Fig. 1) and taking the Fourier transformation of the product $\hat{j}_1\rho_P$, one gets the exchange potential part as

$$U_{\mathrm{Ex}}(\vec{R},\beta) = 32\pi \sum_{\ell=0}^{\infty} \mathrm{Y}_{\ell,0}(\vec{R}\cdot\hat{\Omega}) cg(E) \int ds s^2 j_0\left(\frac{k(R)s}{M}\right) \times V_{Ex}(s) \int dk k^2 j_\ell(kR)\left[A_T^1(k,s)A_P^1(k,s) - \gamma\left(A_T^2(k,s)A_P^1(k,s) + A_T^1(k,s)A_P^2(k,s)\right)\right] \quad (17)$$

The one- and two-dimensional integrals, $A_P^1(k,s)$ and $A_T^1(k,s)$ are given, respectively, as

$$A_P^1(k,s) = \int dx_1 x_1^2 \rho_P(x_1)\hat{j}_1(k_{\mathrm{eff}}^P s) j_0(kx_1).$$
$$A_T^1(k,s) = 2\pi \int_0^\infty dy y^2 j_\ell(ky) \int_{-1}^1 dx \rho_T(y,x) \times \hat{j}_1\left(k_{\mathrm{eff}}^T(y,x)s\right)Y_{\ell,0}(x) \quad (18)$$

where $x \equiv \cos\theta$. The integrals $A_P^2(k,s)$ and $A_T^2(k,s)$ are similar to those given by Eq. (18) but they involve squared projectile and target densities, respectively. Again, the integrals $A_i^n(k,s)$, $i = P,T$ and $n = 1,2$, are assumed to be calculated only once for a given reaction where they are independent of both the separation distance and the orientation angle. This turns out the time-consuming iterated self-consistent calculations of $U_{\mathrm{Ex}}$ at several values of separation distance and different orientations to be rather fast. The total HI potential is then obtained by adding the nuclear, direct plus exchange, parts to the Coulomb one. The matter and charge density distributions of the deformed target nucleus are assumed in the two-parameter Fermi shape,

$$\rho_T(r,\theta_2) = \rho_0^T/(1 + e^{[r - R_T(\theta_2)]/a_T}), \quad (19)$$

where the half-density radius in presence of the quadrupole ($\beta_2$), octupole ($\beta_3$), and hexadecapole ($\beta_4$) deformations is given by

$$R_T(\theta_2) = R_{0T}[1 + \beta_2 Y_{20}(\theta_2) + \beta_3 Y_{30}(\theta_2) + \beta_4 Y_{40}(\theta_2)]. \quad (20)$$

The angle $\theta_2$ is measured from the symmetry axis of the deformed nucleus and the central matter (charge) density, $\rho_0^T$, is determined from the conservation condition

$$\int \rho_T(\vec{r})d\vec{r} = A_T(Z_T), \quad (21)$$

where $A_T(Z_T)$ is the mass (charge) number of the target nucleus. The deformed nucleus density distribution in its two-parameter Fermi form allows us to include the different multipole deformations into the expressions of the direct, Eq. (13), and exchange, Eq. (17), potential parts without

complicating the numerical calculations. For the spherical projectile nucleus we shall use the same two-parameter Fermi form, to express its matter (charge) density distribution, but with constant half-density radius, $R_P$, value. The density distribution parameters for $^{48}$Ca are chosen to verify its root-mean-square radius calculated in the framework of the relativistic mean-field theory [41]. We take the half-density radius parameter, $R_{0T}$, of $^{244}$Pu according to Refs. [24,25,27].

## III. RESULTS AND DISCUSSION

To study the orientation behavior of the Coulomb barrier of two interacting nuclei in clear, we use the microscopic $NN$ effective interaction (M3Y-Paris) characterized by finite range direct and exchange parts. The exchange part has a longer force range term, 1.414 fm, than the ranges of the direct part terms, 0.25 and 0.4 fm, Eqs. (7) and (8). We begin with the case of pure quadrupole deformation, which has a wider value range [42] than that of the higher multipole deformations. Figures 2(a) and 2(b) illustrate the changes of the barrier height ($V_b$) and barrier radius ($R_b$), respectively, for the reaction $^{48}\text{Ca} + {}^{244}\text{Pu} \rightarrow {}^{292}114$ with respect to the quadrupole deformation parameter value, $\beta_2$, at different orientations of the deformed target nucleus (54.7°, 60°, 70°, 80°, and 90°). We have performed our calculations in the double-folding model framework using the direct and

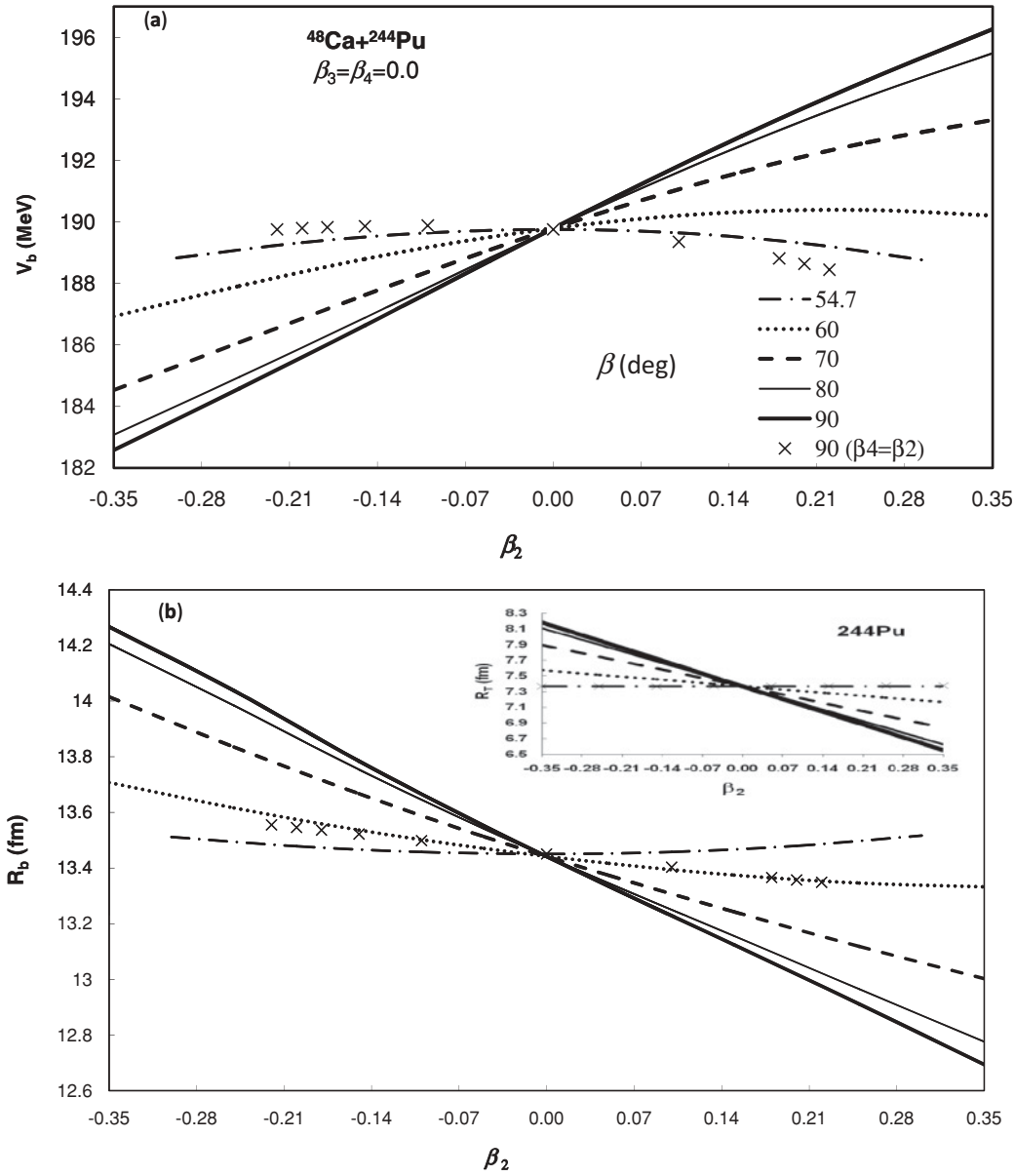


FIG. 2. The variation of the Coulomb barrier (a) height, $V_b$, and (b) radius, $R_b$, for the interacting pair $^{48}\text{Ca} + {}^{244}\text{Pu}$ relative to the quadrupole deformation parameter, $\beta_2$, at different orientation angles, $\beta$ (degrees), of the symmetry axis of the deformed target nucleus $^{244}$Pu. The HI interacting potential is calculated using the direct and exchange parts of the density dependent M3Y *NN* finite range force, BDM3Y1. The inset shows the variation half-density radius of the interacting deformed target nucleus, $^{244}$Pu, at the same orientations.

exchange parts of the HI interaction nuclear potential given by Eqs. (13) and (17), respectively, together with the density dependent finite range force (BDM3Y1), Eqs.(7)–(9). The change of the half-density radius of $^{244}$Pu, relative to the same considered values of the quadrupole deformation and orientations presented in Figs. 2(a) and 2(b) is added to Fig. 2(b) as a guide. At orientations $\beta \geqslant 70^\circ$, Figs. 2(a) and 2(b) show that $V_b$ and $R_b$, respectively, have nearly linear dependence on the quadrupole deformation, $\beta_2$. The barrier height, $V_b$, increases with increasing $\beta_2$, going from the oblate shape into the prolate one, while the barrier radius, $R_b$, decreases. This linearity is shown more clearly for oblate deformations and for the change of the barrier radius. It becomes perfect at $\beta \geqslant 80^\circ$. For orientations $\beta < 70^\circ$ there is direct (reverse), but not linear, dependence for $V_b$ ($R_b$) on $\beta_2$. This dependence decreases till it becomes minor or almost vanishes at the orientation $\beta = 54.7^\circ$ where the Coulomb barrier parameters, $V_b$ and $R_b$, become independent of the quadrupole deformation. We would like to remark that the spherical harmonics, $Y_{20}$ [cos($\beta$)], which define the variation of the half-density radius of the deformed nucleus, denoted in Fig. 1 by $R_T(\beta)$ and given by Eq. (20) replacing $\theta_2$ by $\beta$, has a zero value at $\beta = 54.7^\circ$. Also, the Coulomb barrier parameters exhibit a weak dependence on the deformation parameters at the orientation $\beta = 90^\circ$ when $\beta_2 = \beta_4$. The deformed nucleus at these conditions has a fixed radius, Eq. (20). So, it is of interest now to compare the variation of the Coulomb barrier parameters and that of the half-density radius, $R_T(\beta)$, of the deformed target nucleus, inset of Fig. 2(b), with respect to the quadrupole deformation at the different orientations. As can be seen, both the variation of the Coulomb barrier radius and that of the deformed target radius, in the direction of the separation vector joining the centers of mass of the interacting nuclei, have similar behaviors in the orientation degrees of freedom. The Coulomb barrier height, $V_b$, does the same but with opposite dependence. Here, "opposite" means that there is anticorrelation between $V_b$ and $R_T(\beta)$.

Now, one of the great interests of studying the orientation and deformation dependences of the Coulomb barrier is to determine the optimum orientations for compact and elongated configurations leading to hot and cold fusion reactions, respectively. Figure 2(a) shows that the barrier height curve corresponding to the orientation $\beta = 90^\circ$ is the highest for all positive $\beta_2$ values, prolate nucleus, and vice versa for the barrier radius curve at the same orientation, Fig. 2(b), it is the lowest. So, the compact configuration, with the highest Coulomb barrier and smallest barrier radius, for a prolate nucleus interacting with a spherical one will be at $\beta = 90^\circ$ giving equatorial compact configuration, i.e., in the direction of the minor axis of the deformed nucleus. An equatorial elongated configuration, lowest Coulomb barrier height and largest barrier radius, is obtained in the case of interacting oblate nucleus. It is of interest now to draw firm conclusions about the decisive influence of the variation of deformed nucleus radius on the orientation distribution of the Coulomb barrier if one of the interacting nuclei possesses no purely quadrupole deformation. To do so we plotted in Figs. 3(a) and 3(b) the Coulomb barrier height, $V_b$, and radius, $R_b$, respectively, as a function of the orientation angle of the symmetry axis of the deformed target that has small positive hexadecapole deformation, $\beta_4 = 0.062$, besides the quadrupole one. Four values of quadrupole deformation, $\beta_2 = \pm 0.15, \pm 0.35$, are chosen to simulate intermediate and strong deformations of a prolate and oblate target nucleus. Since both the quadrupole and hexadecapole deformations have reflected symmetry we permit the orientation angle $\beta$ to vary from $0^\circ$ to $90^\circ$. We show in the inset of Fig. 3(b) the change in the $^{244}$Pu half-density radius in the presence of a hexadecapole deformation in addition to the quadrupole one, with the same considered values. The figures show strong orientation dependence of $V_b$ and $R_b$. For a prolate (oblate) deformed nucleus with small positive value of $\beta_4$, the value of $V_b$ varies by about 21.8 MeV (−19.4 MeV) for the value of $\beta_2 = 0.35$ (−0.35) as the orientation angle varies from $\beta = 0^\circ$ to $\beta = 90^\circ$. In the same orientation angle range, the corresponding change in the Coulomb barrier radius, $R_b$, is −2.6 fm (2.2 fm). So, the effect of positive quadrupole deformation is relatively greater than that of the negative one which has the same value. Although there is a slight effect attributed to the folding integrations over the volume of target appearing around the orientation $\beta = 54.7^\circ$, we see that the orientation behavior of $R_b$ follows in a consistent way that of the deformed nucleus radius, see inset of Fig. 3(b), while the behavior of $V_b$ reflexes it inversely. The same correspondence between the orientation behavior of Coulomb barrier parameters and that of deformed nucleus radius has been obtained when the hexadecapole deformation gets larger, $\beta_4 = 0.15$, Figs. 3(c) and 3(d). Actually, for each orientation angle, $\beta$, Figs. 2(b) and 3(b) show an almost constant difference between the Coulomb barrier and the half-density radius of the deformed nucleus, $R_T(\beta)$. This suggests a simple relation between the Coulomb barrier radius, $R_b$, and the half-density radii of the two interacting nuclei, $R_T(\beta)$ and $R_P$, takes the form

$$R_b(\beta) = R_T(\beta) + R_P + \delta, \tag{22}$$

where $\delta$ is a constant independent of the orientation as well as of the target nucleus deformation. For instance, the value of $\delta$ extracted from the calculations presented in Figs. 2(b) and 3(b) is about 2.2 fm and 2.2 ± 0.1, respectively. In fact, the above relation can be expected if we refer to a geometrical consideration of two closely-contacted nuclei interacting with a short-range nuclear interaction having a range of about 1.6 fm. For two interacting nuclei with sharp surfaces, the radius of the Coulomb barrier is expected to be $R_b = R_T + R_P +$ (range of the force). The presence of a finite diffuseness value (≈0.5 fm) increases the value of $R_b$ beyond the nuclear force range. Figure 3(e) shows the behavior of $\delta = R_b(\beta) - R_T(\beta) - R_P$ with the target orientation angle for the calculations presented in Fig. 3(b). As seen in Fig. 3(e), the classical relation, Eq. (22), provides a good description even if the deformed nucleus possesses a weak hexadecapole deformation ($\beta_4 = 0.062$) in addition to its quadrupole one ($\beta_2 = \pm 0.35, \pm 0.15$). The small increase of the value of $\delta$ at the orientations around $\beta = 45^\circ$ is due to the diamond-like shape of the nucleus which has a hexadecapole deformation. At these orientations, the projectile faces flat surface area in the target nucleus which increases the value of the Coulomb radius compared to the case of two curved surfaces. For stronger

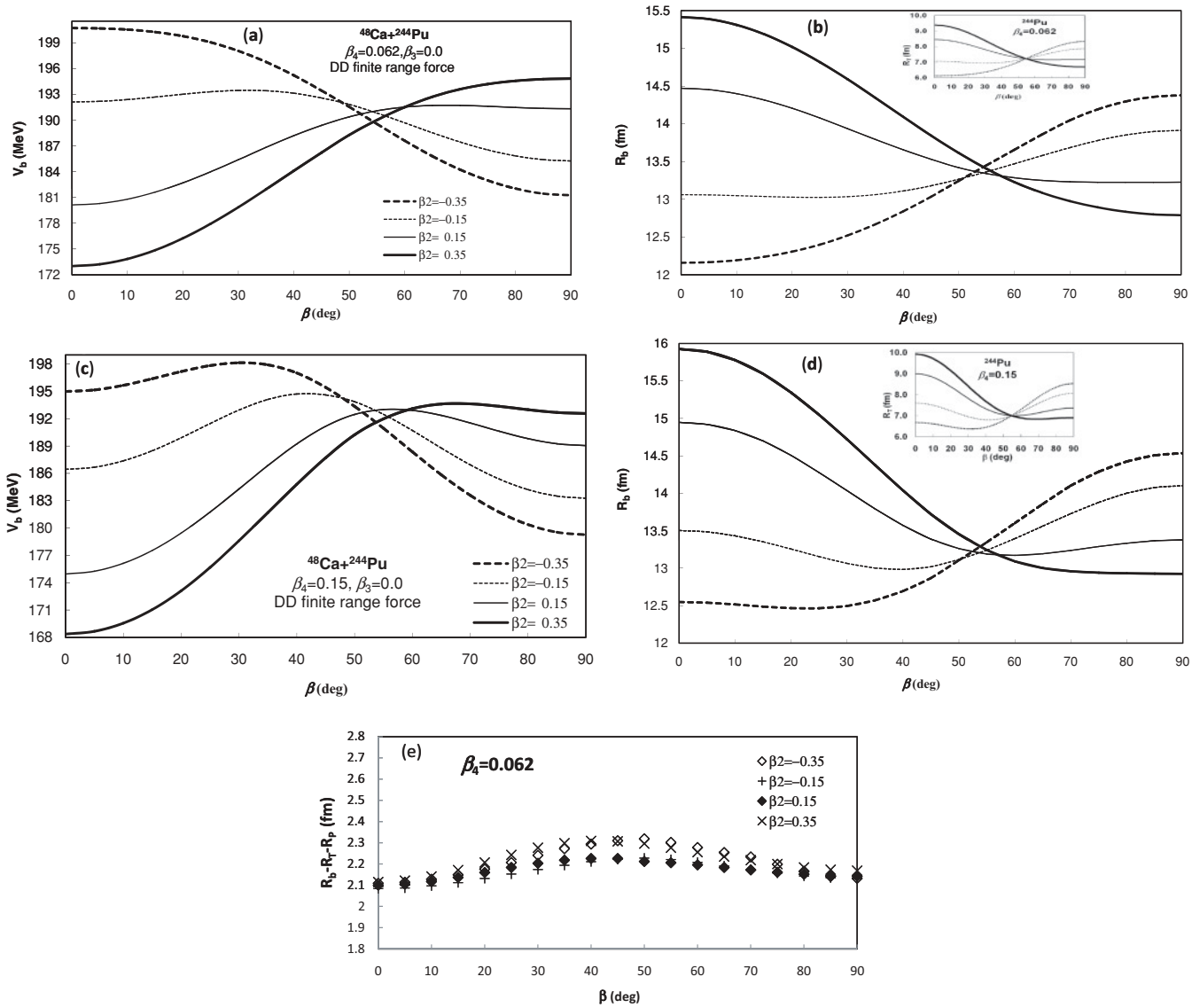


FIG. 3. The distribution of the Coulomb barrier (a) heights, $V_b$, and (b) radii in the orientation degrees of freedom for the interacting pair $^{48}$Ca + $^{244}$Pu. The deformed target nucleus $^{244}$Pu has different quadrupole deformation values in the presence of small positive hexadecapole one, $\beta_4 = 0.062$. The inset shows the orientation variation of the half-density radius for the deformed target nucleus, $^{244}$Pu. (c) and (d) are the same as (a) and (b), respectively, but the deformed nucleus has a large positive hexadecapole deformation, $\beta_4 = 0.15$. (c) shows the variation of the quantity$\delta = R_b(\beta) - R_T(\beta) - R_P$, Eq. (22), with the target orientation angle for the results displayed in (b).

hexadecapole deformation, we found that the points are rather spread out and the classical relation is no longer valid.

Regarding hot and cold fusion processes, presence of the small positive hexadecapole deformation keeps the compact configuration of the deformed prolate nucleus with large quadrupole deformation at $\beta = 90^\circ$ giving an equatorial compact configuration. An elongated configuration is obtained at $\beta = 0^\circ$ (polar elongated configuration). It obtains also the compact configuration of deformed oblate nucleus with large quadrupole deformation at $\beta = 0^\circ$ keeping the elongated configuration at $\beta = 90^\circ$. This is obviously not the case for a deformed target nucleus with weaker quadrupole deformation, $\beta_2 = \pm 0.15$ [Figs. 3(a) and 3(b)], or with stronger hexadecapole deformation, $\beta_4 = 0.15$ [Figs. 3(c) and 3(d)]. Small positive hexadecapole deformation, $\beta_4 = 0.062$, changes the compact configuration in the case of prolate (oblate) deformed nucleus with small quadrupole deformation, $\beta_2 = 0.15$ $(-0.15)$, to be around the orientation $\beta = 67^\circ$ $(\beta = 32^\circ)$. The orientation at which the deformed nucleus has minimum radius value for the same case, inset of Fig. 3(b), is $\beta = 70^\circ$ $(\beta = 31^\circ)$. Larger positive hexadecapole deformation, $\beta_4 = 0.15$, changes the compact configuration in the case of prolate (oblate) deformed nucleus with small quadrupole deformation, $\beta_2 = 0.15$ $(-0.15)$, to be around the orientation $\beta = 57^\circ$ $(\beta = 42^\circ)$ and around the orientation $\beta = 67^\circ$ $(\beta = 30^\circ)$ in the case of large quadrupole deformation, $\beta_2 = 0.35$ $(-0.35)$, Figs. 3(c) and 3(d). The minimum half-density radius of the deformed target nucleus for the

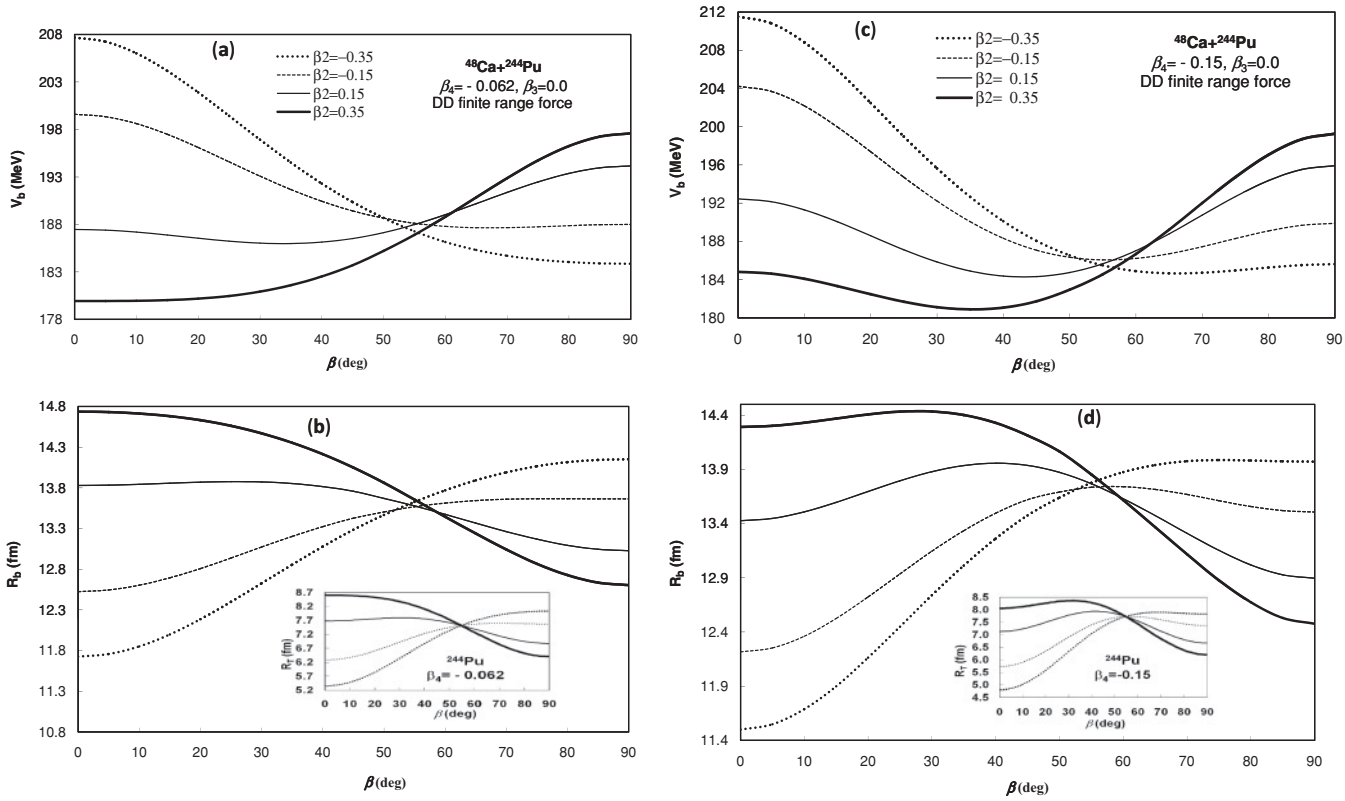


FIG. 4. Same as Fig. 3 but the deformed nucleus has small negative hexadecapole deformation, $\beta_4 = -0.062$ [(a) and (b)] and larger one, $\beta_4 = -0.15$ [(c) and (d)].

same cases, inset of Fig. 3(d), is obtained at orientations $\beta = 57^\circ$ ($\beta = 42^\circ$) and $\beta = 69^\circ$ ($\beta = 32^\circ$), respectively. In this context, it is important to note that the orientation distribution patterns of the Coulomb barrier parameters and those of the deformed nucleus radius, at the different deformations values, are highly analogous to each other. The Coulomb barrier radius (height) pattern agrees (reverses) the deformed nucleus radius one with same (reversed) curvatures and local minima and maxima positions.

Of course, there would be a significant change in the orientation barrier distribution if the hexadecapole deformation is negative instead of the positive one, Figs. 4(a)–4(d). Although the equatorial (polar) compact configuration remains essentially unchanged when the deformed prolate (oblate) nucleus involved in the reaction has, small or large, negative hexadecapole deformation, it is not the case for the elongated one. For instance, the elongated configuration when the prolate nucleus has small quadrupole deformation ($\beta_2 = 0.15$) in addition to a small negative hexadecapole one ($\beta_4 = -0.062$ becomes around the orientation $\beta = 34^\circ$, the deformed nucleus has maximum radius at $\beta = 31^\circ$. Indeed, as the negative hexadecapole deformation gets larger, $\beta_4 = -0.15$, the obtained elongated configuration in case of small prolate (oblate) quadrupole deformation, $\beta_2 = 0.15$ ($-0.15$), changes to be around the orientation $\beta = 43^\circ$ ($56^\circ$), Figs. 4(c) and 4(d). It becomes around the orientation $\beta = 35^\circ$ ($66^\circ$) in the case of larger quadrupole deformation, $\beta_2 = 0.35$ ($-0.35$). The corresponding maximum value for the deformed nucleus radius in these cases, inset of Fig. 4(d), is obtained at $\beta = 42^\circ$ ($57^\circ$) and $\beta = 32^\circ$ ($69^\circ$), respectively. This emphasizes again the similarity between the orientation variation of $R_T(\beta)$ and the corresponding variations of $V_b$ ($\beta$) and $R_b(\beta)$. Moreover, comparing the variations of $V_b$ ($\beta$) and $R_b(\beta)$ for prolate and oblate deformed nuclei with small negative value of $\beta_4$ we note that the orientation response of the oblate nucleus is clearer than that of the prolate one. Also, comparing the same values in case of positive hexadecapole deformation, we would rather conclude that the effect of hexadecapole deformation reinforce (oppose) the orientation quadrupole deformation one if they have same (opposite) signs. This can be seen clearly too if we consider the orientation dependence of the deformed nucleus radius. For example, as the orientation angle varies from $\beta = 0^\circ$ to $\beta = 90^\circ$, the orientation variation of the oblate nucleus with $\beta_2 = -0.35$ decreases from 2.44 fm ($\beta_4 = 0.0$) to 2.20 ($\beta_4 = 0.062$) while the corresponding absolute orientation variation of the prolate nucleus with $\beta_2 = 0.35$ increases from 2.44 fm up to 2.68 fm.

For another trustworthy confirmation of our result concerning the correlation (anticorrelation) of the orientation variation of the Coulomb barrier radius (height) with that of the interacting deformed nucleus radius, we shall consider these variations in the presence of an asymmetry octupole deformation. Figures 5(a) and 5(b) show the orientation distribution of Coulomb barrier parameters, $V_B$ and $R_B$, respectively, when the deformed $^{244}$Pu nucleus has an octupole deformation, $\beta_3$, in addition to its quadrupole and hexadecapole ones, $\beta_2 = 0.25$ and $\beta_4 = 0.062$. Five values of the octupole deformation parameter, $\beta_3 = 0$, $\pm 0.05$ and $\pm 0.1$, are assumed. We permit the orientation angle $\beta$ to vary from $0^\circ$ to $180^\circ$ where the

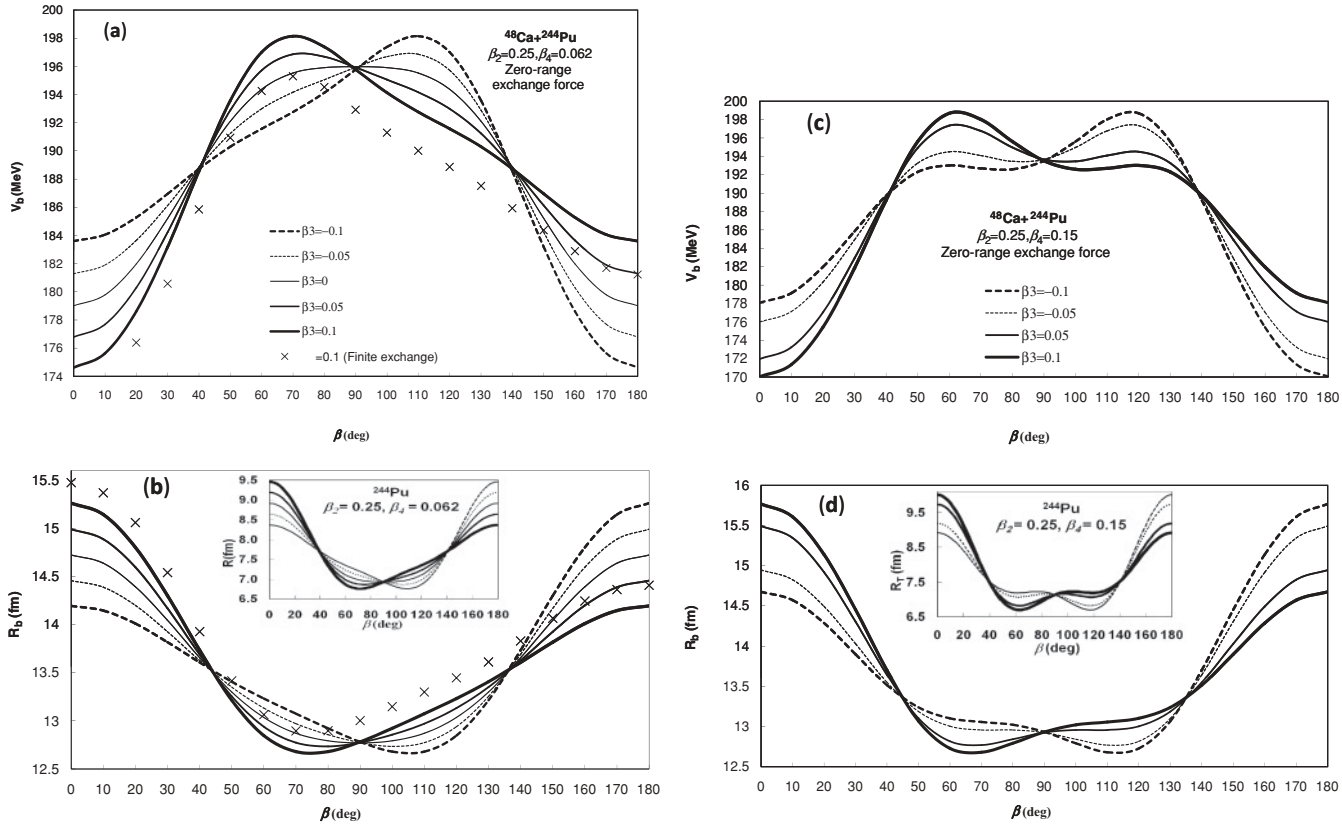


FIG. 5. Same as Fig. 4 but the deformed target nucleus has octupole deformation, $\beta_3$, with different values in addition to its quadrupole deformation ($\beta_2 = 0.25$) and the hexadecapole one with two different values, $\beta_4 = 0.062$ [(a) and (b)] and $\beta_4 = 0.15$ [(c) and (d)]. The calculations are performed using zero-range exchange part of the M3Y *NN* interaction. Also shown are the results for $\beta_3 = 0.1$ obtained with a finite-range exchange part for comparison.

octupole deformation breaks the reflection symmetry of the nucleus. For simplicity, we considered the density dependent M3Y $NN$ force with a zero-range exchange part. The strong dependence of the Coulomb barrier parameters on the octupole deformation is appearing clearly. The absolute maximum variation of the Coulomb barrier height in the mentioned orientation range is 20.1 MeV and 23.5 MeV for $\beta_3 = \pm 0.05$ and $\pm 0.1$, respectively, while it is 17.0 MeV for $\beta_3 = 0$. As can be seen in Figs. 5(a) and 5(b), the Coulomb barrier parameters follow an orientation pattern similar to the deformed nucleus radius one, inset of Fig. 5(b). The inclusion of the octupole deformation with different values of 0.1, 0.05, $-0.05$, and $-0.1$ changes the compact configuration orientation to be at $\beta = 71^\circ$, $73^\circ$, $106^\circ$, and $109^\circ$, respectively. The minimum deformed nucleus radius for these octupole deformation values occurs at $\beta = 71^\circ$, $75^\circ$, $105^\circ$, and $109^\circ$, respectively. The positive (negative) octupole deformation values keep the polar elongated configuration to be at the orientation $\beta = 0^\circ$ ($180^\circ$). To assess the effect of using a zero-range exchange part of the $NN$ interaction instead of the finite-range one on the barrier behavior, the calculations made for the case of $\beta_3 = 0.1$ with the finite-range exchange part are also displayed in Figs. 5(a) and 5(b) for comparison. As seen, the use of the finite-range exchange force reduces the values of the Coulomb barrier height by about 2.1–2.9 MeV increasing the barrier radius by about 0.19–0.26 fm. Fortunately, these changes do not affect the general behavior of the Coulomb barrier parameters in the orientation degrees of freedom, which is the issue of interest here.

Finally, in the case of larger positive hexadecapole deformation ($\beta_4 = 0.15$), Figs. 5(c) and 5(d), the compact configuration is obtained at the orientation $\beta = 62^\circ$ ($\beta = 118^\circ$) in presence of a positive (negative) octupole deformation, irrespective of its value. The corresponding minimum half-density radius is obtained at the orientation $\beta = 63^\circ$ ($\beta = 117^\circ$), inset of Fig. 5(d), which confirms our result.

## IV. SUMMARY AND CONCLUSION

In summary, the orientation distribution of the Coulomb barrier for reactions involving deformed target nuclei is discussed in the context of the folding model formalisms based on the density dependent $NN$ interaction with the direct and exchange parts of finite ranges. We implement folding expressions which can be used to perform the microscopic calculations for the interaction potential between spherical-deformed interacting nuclear pair, containing a self-consistency problem, without consuming computational time. Specifically, we have demonstrated that the orientation variation of the colliding

deformed nucleus radius, in the direction of the separation vector between colliding nuclei, has the substantial role in forming the Coulomb barrier distribution in the orientation degrees of freedom. The orientation dependence patterns of the Coulomb barrier parameters, height and radius, are found to behave in directly (inversely) reasonable agreement with the deformed target radius orientation pattern. Taking advantage of this result, our overall conclusion is that this correlation (anticorrelation) provides a chance to deduce the orientation barrier distribution and the optimum orientations for compact and elongated configurations of colliding nuclei in an acceptable accurate way without performing heavy calculations. Moreover, this correlation (anticorrelation) offers a great help when we need to take into account the orientation degrees of freedom in microscopic calculations instead of calculating the interaction potential several times, up to hundreds of times, as we have to do in the coupled channel calculations. This correlation between the Coulomb barrier and the deformed target nucleus radius can be achieved independently of the $NN$ force used in the calculations. We have used ordinary M3Y-Reid and Paris versions with a zero-range exchange part obtaining the same relation.


[1] D. J. Hinde, R. G. Thomas, R. du Rietz, A. Diaz-Torres, M. Dasgupta, M. L. Brown, M. Evers, L. R. Gasques, R. Rafiei, and M. D. Rodriguez, Phys. Rev. Lett. **100**, 202701 (2008).

[2] Nan Wang, Jun-qing Li, and En-guang Zhao, Phys. Rev. C **78**, 054607 (2008).

[3] V. Zagrebaev and W. Greiner, J. Phys. G: Nucl. Part. Phys. **34**, 1 (2007).

[4] Yu. Ts. Oganessian *et al.*, Phys. Rev. C **76**, 011601(R) (2007).

[5] I. I. Gontchar, D. J. Hinde, M. Dasgupta, C. R. Morton, and J. O. Newton, Phys. Rev. C **73**, 034610 (2006).

[6] M. Manhas and R. K. Gupta, Phys. Rev. C **72**, 024606 (2005).

[7] K. Hagino and N. Rowley, Phys. Rev. C **69**, 054610 (2004).

[8] R. A. Gherghescu, D. N. Poenaru, W. Greiner, and Y. Nagame, J. Phys. G: Nucl. Part. Phys. **32**, L73 (2006).

[9] W. Li, N. Wang, F. Jia, H. Xu, W. Zuo, Q. Li, E. Zhao, J. Li, and W. Scheid, J. Phys. G: Nucl. Part. Phys. **32**, 1143 (2006).

[10] M. Ismail, W. M. Seif, M. M. Osman, H. El-Gebaly, and N. M. Hassan, Phys. Rev. C **72**, 064616 (2005).

[11] V. I. Zagrebaev, Y. Aritomo, M. G. Itkis, Yu. Ts. Oganessian, and M. Ohta, Phys. Rev. C **65**, 014607 (2001).

[12] G. G. Adamian, N. V. Antonenko, and W. Scheid, Nucl. Phys. A **678**, 24 (2000).

[13] W. Reisdorf, J. Phys. G **20**, 1297 (1994).

[14] A. B. Balantekin, A. J. DeWeerd, and S. Kuyucak, Phys. Rev. C **54**, 1853 (1996).

[15] J. G. Keller, K.-H. Schmidt, F. P. Hessberger, G. Munzenberg, and W. Reisdorf, Nucl. Phys. A **452**, 173 (1986).

[16] C. H. Dasso, H. Esbensen, and S. Landowne, Phys. Rev. Lett. **57**, 1498 (1986).

[17] S. Bjørnholm and W. J. Swiatecki, Nucl. Phys. A **391**, 471 (1982).

[18] R. G. Stokstad, Y. Eisen, S. Kaplanis, D. Pelte, U. Smilansky, and I. Tserruya, Phys. Rev. Lett. **41**, 465 (1978).

[19] S. Hofmann and G. Münzenberg, Rev. Mod. Phys. **72**, 733 (2000).

[20] Yu. Oganessian, J. Phys. G: Nucl. Part. Phys. **34**, R165 (2007).

[21] S. Hofmann *et al.*, Eur. Phys. J. A **32**, 251 (2007).

[22] C. Y. Wong, Phys. Rev. Lett. **31**, 766 (1973).

[23] J. Blocki, J. Randrup, W. J. Swiatecki, and C. F. Tsang, Ann. Phys. (NY) **105**, 427 (1977).

[24] R. K. Gupta, M. Balasubramaniam, R. Kumar, N. Singh, M. Manhas, and W. Greiner, J. Phys. G: Nucl. Part. Phys. **31**, 631 (2005).

[25] R. K. Gupta, M. Manhas, and W. Greiner, Phys. Rev. C **73**, 054307 (2006).

[26] M. Manhas and R. K. Gupta, Phys. Rev. C **72**, 024606 (2005).

[27] M. Manhas, Raj K. Gupta, Q. Li, S. K. Patra, and W. Greiner, Phys. Rev. C **74**, 034603 (2006).

[28] R. K. Gupta, N. Singh, and M. Manhas, Phys. Rev. C **70**, 034608 (2004).

[29] M. Ismail, W. M. Seif, and M. M. Botros, Nucl. Phys. A **828**, 333 (2009).

[30] M. Seiwert, N. Abul-Naga, V. Oberacker, J. A. Maruhn, and W. Greiner, Gesellschaft für schwerionenforschung, GSI, Annual Report, 1981.

[31] R. K. Gupta, M. Manhas, G. Münzenberg, and W. Greiner, Phys. Rev. C **72**, 014607 (2005).

[32] Yu. Ts. Oganessian *et al.*, Phys. Rev. C **69**, 054607 (2004); **70**, 064609 (2004).

[33] Dao T. Khoa and W. von Oertzen, Phys. Lett. B **342**, 6 (1995).

[34] N. Anantaraman, H. Toki, and G. Bertsch, Nucl. Phys. A **398**, 269 (1983).

[35] G. R. Satchler and W. G. Love, Phys. Rep. **55**, 183 (1979).

[36] L. J. B. Goldfarb and P. Nagel, Nucl. Phys. A **341**, 494 (1980).

[37] M. Ismail, W. M. Seif, and H. El-Gebaly, Phys. Lett. B **563**, 53 (2003).

[38] X. Campi and A. Bouyssy, Phys. Lett. B **73**, 263 (1978).

[39] Dao T. Khoa, Phys. Rev. C **63**, 034007 (2001).

[40] P. Ring and P. Schuck, *The Nuclear Many-Body Problem* (Springer-Verlag, New York, 1980), p. 542.

[41] G. A. Lalazissis, S. Raman, and P. Ring, At. Data Nucl. Data Tables **71**, 1 (1999).

[42] S. Raman, C. W. Nestor Jr., and P. Tikkaneny, At. Data Nucl. Data Tables **78**, 1 (2001).